ChemElectroChem

Research Article
doi.org/10.1002/celc.202400663

Chemistry Europe
European Chemical Societies Publishing

www.chemelectrochem.org

Two-Dimensional Titanium Disulfide Nanosheets for Enhanced Capacity of Zinc-Ion Capacitors

Sumeyye Kandur Baglicakoglu,[a] Sena Oz,[a] Ali Deniz Ucar,[a] Yusuf Kocak,[b] Mete Batuhan Durukan,[a] Emrah Ozensoy,[b, c] and Husnu Emrah Unalan*[a, d]

Capacitors offer high power density, superior cycle stability, and fast charging, making them highly promising for energy storage. However, their energy density needs to be improved. Due to zinc's abundance, low cost, high capacity, and stability, aqueous zinc-ion capacitors have garnered significant attention. Zinc-ion capacitors (ZnCs) face challenges such as rapid capacity decrease and reduced lifespan due to strong electrostatic interactions, electrode material dissolution, and sluggish ionic diffusion. Bulk titanium disulfide (TiS_2) has been investigated as an electrode material to overcome these disadvantages, but the effects of its two-dimensional (2D) structure have yet to be discovered. With this work, preliminarily fabricated bulk TiS_2 is exfoliated into a semi-metallic 2D TiS_2 nanosheets using organolithium chemistry, optimizing it as a ZnC cathode material to enhance energy density. The 2D-TiS_2 exhibited a specific capacitance of 214.3 $F g^{-1}$ at 0.1 $mV s^{-1}$ scan rate and a specific capacity of 116.4 $mAh g^{-1}$ at 0.1 $A g^{-1}$ current density while significantly outperforming bulk TiS_2. This work highlights the potential of 2D-TiS_2 to enhance the energy density of ZnCs through improved electrical conductivity and improved accessibility of ions through nanosheets, offering a new class of cathodes for enhanced energy storage.

Introduction

Energy demand has increased drastically due to the growing use of electronic devices, electric vehicles, and industrialization. This energy demand is met with non-renewable energy sources, such as oil, natural gas, and coal.[1] These fossil fuels also release harmful pollutants, increasing the carbon footprint.[2,3] To address this, increasing the dependence on renewable energy production and storage, such as wind and solar energy harvesting, has become compulsory.[4,5] However, discontinuous and sometimes interrupted renewable energy sources become a significant obstacle at that point. To overcome that obstacle, electrochemical energy storage systems come into play in long and short-term storage applications at large-scale grid applications and small-scale personal microelectronic applications.[6,7] Electrochemical energy storage systems, such as batteries and supercapacitors, are increasingly used in electric vehicles,[8] wearable electronic technologies,[9] memory backup systems, smart grids, and microelectronic devices[10–12] due to their high power and energy densities[13] and long operational lifetimes.

Derivatives of transition metals such as cobalt (Co),[14] nickel (Ni),[15] manganese (Mn),[16] iron (Fe)[17] and carbonaceous materials[18–20] such as activated carbon (AC),[21] graphite[22] and graphene[23] have been widely integrated into electrochemical energy storage devices.[24–28] Transition metal oxides such as MnO_2 have been also used as a cathode material in energy storage systems like Zinc ion batteries. They offer a cost effective and eco-friendly alternative while facing some obstacles such as manganese dissolution and low conductivity.[29] In addition to these materials, MXenes, a family of 2D carbides, nitrides, and carbonitrides, have emerged in electrochemical energy storage.[30] The advantages of 2D structures, such as high specific surface area and short ion transport pathways, are particularly emphasized in MXenes.[31,32] These characteristics allow for rapid charge and discharge cycles, which are crucial for energy storage devices.[33] MXenes are known for their electrical conductivity, hydrophilicity, and large surface area. These properties make MXenes particularly appropriate for applications in supercapacitors and other energy storage devices.[34] The unique layered structure of MXenes allows rapid ion transport and high charge storage capacity, addressing some of the limitations faced by traditional materials.[35] Analogous to MXenes and other 2D materials, transition metal dichalcogenides (TMDs) have drawn significant attention due to their layered structure, which gives rise to the desired electrochemical properties.[36,37] TMDs have a layered structure resulting from bonding a transition metal (e.g., molybdenum (Mo), titanium (Ti), and niobium (Nb), tungsten (W), etc.) with a chalcogenide such as (sulfur (S), selenium (Se), and tellurium (Te)).[38,39] While strong covalent bonds form the layers, weak Van der Waals bonds are observed between the layers.[40] By

[a] S. K. Baglicakoglu, S. Oz, A. D. Ucar, M. B. Durukan, H. E. Unalan
Department of Metallurgical and Materials Engineering, Middle East Technical University (METU), 06800, Ankara, Türkiye

[b] Y. Kocak, E. Ozensoy
Department of Chemistry, Bilkent University, 06800 Ankara, Türkiye

[c] E. Ozensoy
UNAM-National Nanotechnology Center, Bilkent University, 06800, Ankara, Türkiye

[d] H. E. Unalan
Energy Storage Materials and Devices Research Center (ENDAM), Middle East Technical University (METU), 068000, Ankara, Türkiye
E-mail: unalan@metu.edu.tr

Supporting information for this article is available on the WWW under https://doi.org/10.1002/celc.202400663

breaking these weak Van der Waals bonds, layered materials can be obtained as 2D structures for intriguing electrochemical applications, mainly energy storage.[41] The most common TMDs used in these systems are molybdenum disulfide (MoS_2),[41] tungsten disulfide (WS_2),[42] and molybdenum diselenide ($MoSe_2$).[43]

The lightest and pioneer member of the family in the scope of intercalation energy storage is titanium disulfide (TiS_2). One of the earliest demonstrations of lithium intercalation was done by Stanley Whittingham, who proposed TiS_2 as an energy storage material. Studies on TiS_2, which have also been the subject of intercalation studies due to their structural properties, have lost momentum in subsequent periods.[44] Years later, although TiS_2's properties include fast ion transportation and effective diffusion capabilities, its application area remains limited due to thermodynamic limitations and oxidation problems coupled with releasing toxic hydrogen sulfide (H_2S) gas.[45,46] TiS_2 possesses many advantages in energy storage, such as high energy density, fast ion transport rate, minimal volume change during reversible charge-discharge cycles, and structure maintenance during ion intercalation.[47] In its bulk form, TiS_2 exhibits semiconductor properties, and when formed in 2D nanosheets, it has been shown to have a bandgap ranging from 0.5 to 1.2 eV.[48,49] This bandgap change enables its use in various fields and enhances its performance in electrochemical applications.[50]

After being neglected for several decades, TiS_2 came into play in various types of batteries and high-rate capacitors.[51] Due to its unique properties, the recent popularity of TiS_2 for energy storage applications has created a need for comprehensive analysis and comparative information. Supercapacitors are a good substitute for energy storage due to their high-power density, superior cycle stability, and fast charging. Nevertheless, the energy density still needs to be improved. To overcome this, hybrid supercapacitors (HSCs) have been developed by combining two types of electrodes – a capacitor and a battery. Zinc capacitors (ZnCs) are a competitor for this kind of capacitor application due to Zn's abundance, cost-effectiveness, high theoretical capacity, and exceptional stability, offering potential advantages over LIBs regarding safety, affordability, and environmental friendliness.[52,53] However, ZnCs encounter significant challenges hindering their practical applications. Strong electrostatic interactions between zinc ions and electrode materials can lead to rapid capacity decrease and reduced battery lifespan. However, electrode material dissolution and sluggish ionic diffusion further limit performance and cycle stability.[54] Innovative approaches to electrode design and electrolyte optimization are necessary to address these issues. Notably, while Zn metal is commonly used as the anode in ZIBs, its thermodynamic instability and dendrite formation pose challenges.[55] Nevertheless, the search for materials with strong cycle ability and fast reaction kinetics is made more difficult by the electrostatic interaction between divalent zinc ions and host structures. This research aims to explore the potential of TiS_2, traditionally a cathode material, by also comparing its bulk and 2D forms' electrochemical performances.

Experimental Section

Materials

Titanium (99.9%) powder was obtained from Nanografi Co. Inc. Sulfur (99.98%) powder, n-butyllithium (1.6 M in Hexane), carbon black (CB), poly(vinylidene) fluoride (PVDF), N-methyl-2-pyrolidone (NMP) and sodium dodecyl sulfate (SDS, 99.0%) were purchased from Sigma Aldrich, respectively. Single-walled carbon nanotubes (P3-SWCNTs) were purchased from Carbon Solutions Inc. Hydrophobic polytetrafluoroethylene filter membranes (PTFE, 0.45 μm pore size, 47 mm diameter) from ISOLAB. 20 μm thick Zn (99.99%) foils were purchased from Aliexpress.

Fabrication of 2D-TiS_2 Nanosheets

Fabrication of bulk and 2D TiS_2 was done according to an earlier work.[56] Shortly, Ti and S powders are mixed in stoichiometric amounts and subjected to annealing at 650 °C for 18 hours in a vacuum-sealed quartz tube. Resulting bulk TiS_2 powders are used without post-processing. 0.5 grams of the resulting TiS_2 powder are mixed with 10 ml of n-butyllithium and stirred in a sealed autoclave at 80 °C for 48 hours in the glove box. The lithium-intercalated TiS_2 powders are then washed by centrifugation three times with hexane, ethanol, and deionized water at 11,000 rpm for 30 minutes. Afterward, the powders are dispersed in 300 ml of deionized water and ultrasonicated in an ice bath for 4 hours. The product is then washed twice with water and transferred to ethanol. Determination of concentration is conducted via weighing the filter papers prior to and after filtration of 10 ml of TiS_2 suspension. Then, the final concentration is arranged to 1 $mg.ml^{-1}$, finally stored in ethanol for future use.

Fabrication of Self-Standing 2D-TiS_2 Films and Device Assembly

0.125 g of SDS was dissolved in 100 ml of deionized water using a tip sonicator for 10 minutes. Next, 20 mg of SWCNTs was added to the SDS solution and sonicated for an additional 5 minutes to achieve proper dispersion. Following this, 15 ml of the SWCNT solution was slowly added to 30 ml of a 1 $mg.ml^{-1}$ concentrated TiS_2 solution while stirring vigorously at room temperature for 1 hour. The resulting mixture was then vacuum filtered using hydrophobic PTFE membrane filters to obtain self-standing, flexible TiS_2 films.

Fabrication of Bulk-TiS_2 Electrodes

Bulk-TiS_2 electrodes are prepared via a traditional slurry method. 85 wt% active material (bulk TiS_2), 10 wt% carbon black (CB), and 5 wt% PVDF are ready with NMP to obtain a paste-like slurry. This slurry was coated onto the stainless-steel substrates by a simple doctor-blading method. The electrodes are then vacuum-dried at 80 °C overnight to ensure complete evaporation of the NMP.

Material Characterization

X-ray diffraction (XRD) analysis is carried out using a Rigaku D/Max-2000 diffractometer with Cu Kα radiation, operating at 40 kV, over a 10–90° range and a 1° min^{-1} scanning rate. Electrochemical activation of 10 cyclic voltammetry cycles is done before XRD analysis to observe the structural changes. Afterward, they were subjected to specific voltages where redox peaks were observed. The samples were washed gently with deionized water (DI) and

dried in a vacuum furnace at room temperature before XRD analysis. Conductivity measurements were performed using a Signatone Pro4 4-point probe testing station connected to a Keithley 2400 sourcemeter. Raman spectra is recorded using a BRUKER FRA 106/S spectrometer with an excitation laser wavelength of 532 nm. Scanning electron microscopy (SEM) analysis was conducted with an FEI Nova Nano FEG-SEM operating at 20 keV. Transmission electron microscopy (TEM) samples were prepared by drop-casting diluted TiS_2 suspension onto holey carbon-coated 400 mesh copper grids. High-resolution TEM (HR-TEM JEOL JEM-2100F) and high-contrast TEM (HC-TEM FEI Tecnai G2 Spirit BioTwin) analyses were performed at 200 and 120 kV operating voltages. X-ray photoelectron spectroscopy (XPS) experiments were conducted with a SPECS HSA3500 hemispherical energy analyzer and a PHOIBOS 100 detector with an MCD-5.

Electrochemical Characterization

Electrochemical measurements were performed using a VMP-3 Biologic potentiostat/galvanostat system. Self-standing 2D-TiS_2 films were punched into 21 mm diameter electrodes. Zn foils were used as the anode, and fabricated self-standing 2D TiS_2 films are used as cathodes with 2 M of $ZnSO_4$ as the electrolyte. Glass fibers were used as separators, which were wetted before the assembly of the cells. 2032-coin cells were used to obtain ZnCs. Bulk-TiS_2 electrodes were assembled in the same way for electrochemical analysis.

Results and Discussion

To prepare bulk TiS_2 powder, stoichiometrically mixed Ti and S powders were first annealed in a vacuum-sealed quartz tube. Organolithium exfoliation, a widely used technique for fabrication of 2D-TMDs, was applied to the resultant bulk powder. Lithium hydroxide (LiOH) and hydrogen gas (H_2) were produced when Li^+ ions intercalate and react with water molecules during sonication.[57,58] Semi-metallic 2D TMDs were produced when this reaction separated 2D sheets, causing quantum confinement.[59] Furthermore, the van der Waals forces between the layers were weakened by the intercalation of lithium and the emission of H_2 gas, increasing the interlayer separation. After that, the 2D-TiS_2 solution was vacuum-filtered to fabricate binder-free and self-standing electrodes, which do not require conductive additives due to their inherent electrical conductivity. SWCNTs were added to these TiS_2 sheets to improve the mechanical stability and ease the handling of the self-standing electrodes.

Figure 1a shows the bulk TiS_2 powders after annealing in the vacuum-sealed quartz tubes. As expected, hexagonal crystal formations can be observed. Resultant powders were exfoliated via organolithium chemistry, leading to 2D-TiS_2 suspension in ethanol, which can be vacuum-filtrated to obtain self-standing films. Fabricated films were approximately 20 μm thick (Figure 1b). Large 2D sheets with more than 20 μm lateral diameters were formed following the organolithium exfoliation, indicating a successful exfoliation process (Figure 1c). Energy dispersive X-ray spectroscopy (EDX) mapping was conducted on the films, yielding a homogeneous dispersion of Ti and S (Figure 1d). With the SWNCT addition, vacuum-filtrated films were flexible enough to bend (Figure 1e-i and 1e-ii). The electrical resistance of the 2D-TiS_2 self-standing films is also measured simply with a multimeter, showing less than 17 ohms in 47 mm, indicating the excellent conductivity of 2D-TiS_2 nanosheets. With a 4-probe approach, the films' sheet resistance was found to be 4.7 ± 0.3 Ohm/sq, further supporting the feasibility of the organolithium exfoliation to obtain electrically conductive 2D-TiS_2 nanosheets.

Figure 2a shows the XRD patterns of bulk TiS_2 and 2D-TiS2 nanosheets. The bulk TiS_2 XRD pattern matched the typical hexagonal pattern (JCPDS card no. 88-1967). A prominent, distinctive peak at 15.85° (001) was expanded during organolithium exfoliation, indicating a cleavage through the axis due to decreased scattering volume within structure.[60] However, other peaks disappeared due to exfoliation, suggesting cleavage along the (001) and confirming few-layered structure of 2D-TiS_2. The Raman spectra displayed two prominent peaks at 331 and 371 (with 371 cm^{-1} being a shoulder peak for 2D-TiS_2 designated as 'sh'), as seen in Figure 2b. The peak at 331 cm^{-1} corresponds to the Raman active mode of TiS_2 A_{1g} (out-of-plane) mode. The intensity ratio of the A_{1g} to the shoulder peak was determined to be 2, suggesting a structure consisting of 2 to 4 layers.[61] This Raman analysis confirmed the 2D nature of TiS_2, which is in line with XRD results in Figure 2a. XPS analysis was also done to understand the change in the surface chemistry of TiS_2 after the organolithium exfoliation. The general XPS spectra showing both bulk TiS_2 and 2D-TiS_2 were provided in Figure 2c. There was no distinct difference between the two, indicating a successful exfoliation of TiS_2 structures. Additionally, the absence of Li peaks in the 2D-TiS_2 spectrum proves a complete removal of the lithium compounds during the exfoliation and centrifugation. There was no distinct difference between the bulk and 2D structures when the Ti_{2p} region was analyzed (Figure 2d). The characteristic peaks at 458.6 eV ($2p_{3/2}$) and 464.3 eV ($2p_{1/2}$) correspond to Ti^{+4} species of TiS_2 structure.[62] Another peak at 458.6 eV can be attributed to TiO_2, which can be attributed to surface-limited oxidation due to water, moisture, or air exposure[61] which showed similar characteristics in both samples. Additionally, in both the bulk and 2D samples, the dominant sulfur species was S^{2-}.[63] In the literature, S^{2-} signals at higher binding energy values have been associated with a defective TiS_2 structure, which can be correlated with the exfoliation procedure in this case.[64–66] In Figure 3d–e, the peak associated with S2p3/2 at 160.7 eV for bulk TiS_2 shifts to 160.8 eV for 2D-TiS_2, while the S2p1/2 peak at 161.8 eV for bulk TiS_2 shifts to 162.0 eV for 2D-TiS_2. These shifts to higher binding energies are consistent with previous literature,[67,68] indicating structural modifications due to exfoliation. In Figure 2f, the O1s signals observed at 530.3 eV and 530.1 eV in the bulk and 2D structures belong to TiO_2 species due to partial surface oxidation of TiS_2.[69] All in all, XRD and Raman characterizations confirm the formation of few-layered nanosheets with organolithium exfoliation. At the same time, the XPS verifies the existence of partial oxidation, which is limited to the surface of the TiS_2 nanosheets. This argument is also supported by XRD signals in Figure 2a that showed no distinct TiO_2 peaks since the oxidation is limited to the surface of the nanosheets.[70]

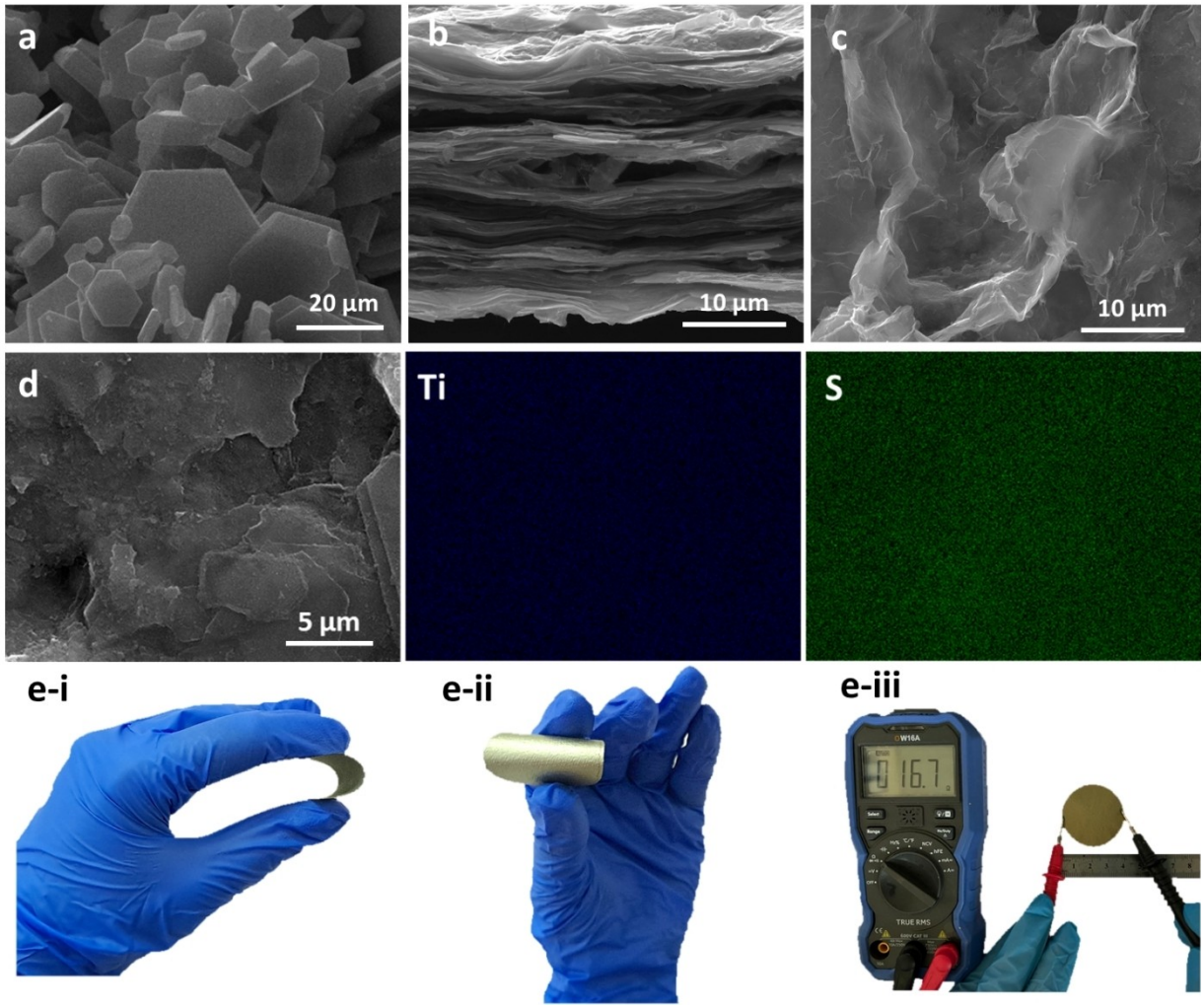

Figure 1. SEM images of (a) bulk TiS_2, (b) cross-section of self-standing 2D-TiS_2 films, (c) 2D TiS_2 nanosheet edges. (d) SEM imaging of the top of the self-standing film and relevant EDX mappings. e) Photos of self-standing film showcasing the i, ii) flexibility, and iii) low electrical resistance.

The electrochemical measurements were conducted in a half-cell configuration where Zn acted as anode, TiS_2 as cathode, and 2 M $ZnSO_4$ as the electrolyte. Results were given in Figure 3. CV measurements are performed at various scan rates within a potential window of 0–1 V for the cells, the results of which were provided in Figures 3a and 3b. Specific capacitance values were calculated from the CV graphs, and 2D-TiS_2-based ZnCs were found to have a specific capacitance of 214.3 $F g^{-1}$ at a scan rate of 0.1 $mV s^{-1}$. On the contrary, bulk TiS_2-based ZnCs had a specific capacitance of only 73.86 $F g^{-1}$, clearly showing higher performance of 2D nanosheets. The comparison in the performance can be clearly observed in Figure 3c. At low scan rates, distinct redox peaks were observed at different voltages, clearly showing the system's faradaic mechanism. Many redox couples were observed during the cathodic/anodic scan, indicating the gradual insertion and extraction of Zn cations into and out of TiS_2. Compared at a scan rate of 0.1 $mV s^{-1}$, 2D-TiS_2 nanosheets clearly showed both more significant capacitive region on top of much more active faradaic reactions. This can be attributed to the much more accessible layers for Zn^{2+} intercalation due to the exfoliation, aside from the excellent conductivity of the self-standing 2D-TiS_2 films.

Although the reaction mechanisms of faradaic peaks remained elusive, the overall interaction of Zn and TiS_2 can be written as follows:[71]

$$\text{Anode}: \quad Zn \leftrightarrow Zn^{2+} + 2e^-$$

$$\text{Cathode}: \quad TiS_2 + xZn^{2+} + 2xe^- \leftrightarrow Zn_xTiS_2$$

Galvanostatic charge-discharge measurement (GCD) was also conducted on 2D-TiS_2-based ZnCs, and charge-discharge curves at different current densities were provided in Figure 3d. Both charge and discharge curves have numerous slope changes, indicating the complex reactions of 2D-TiS_2-based ZnCs shown in Figure 3c. The 2D structure showed more dominant redox peaks as a result of the creation of more active sites for chemical reactions to take place.[72–74] A maximum specific capacity of 116.4 $mAh g^{-1}$ was achieved at a current

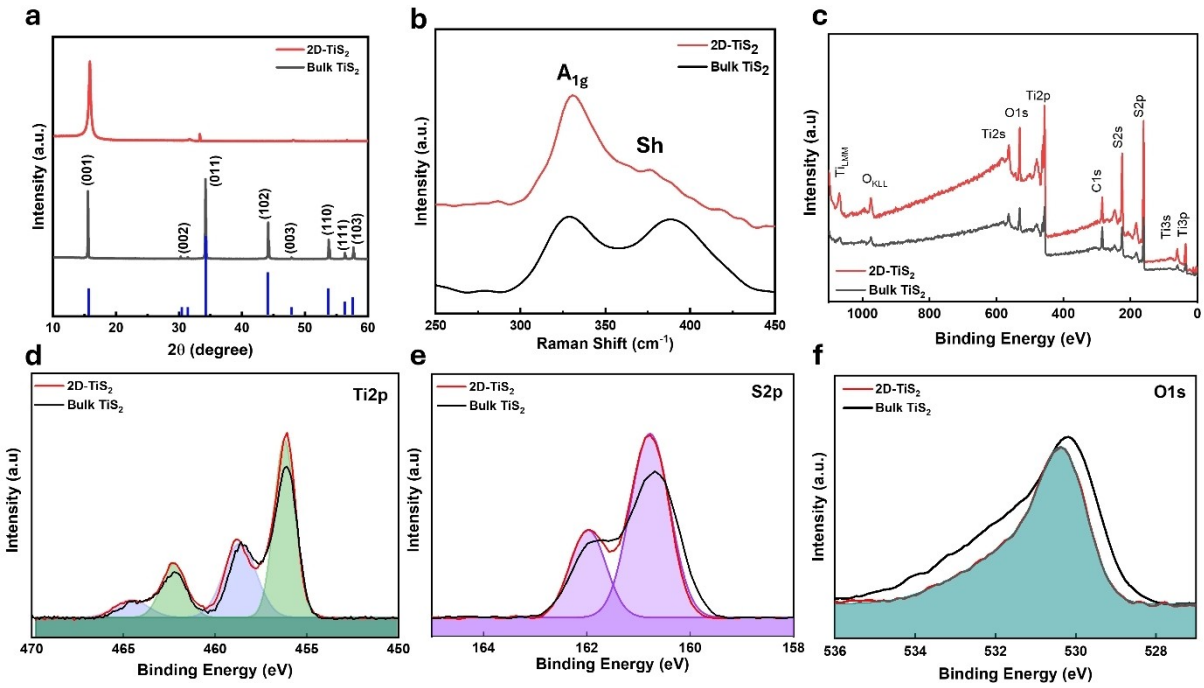

Figure 2. Physiochemical characterizations of bulk and 2D-TiS_2. Comparisons of a) XRD patterns, b) Raman spectra, and c) XPS spectra of bulk TiS_2 powders and 2D-TiS_2 nanosheets. XPS spectra of d) Ti_{2p}, and e) S_{2p}, and O_{1s} bondings.

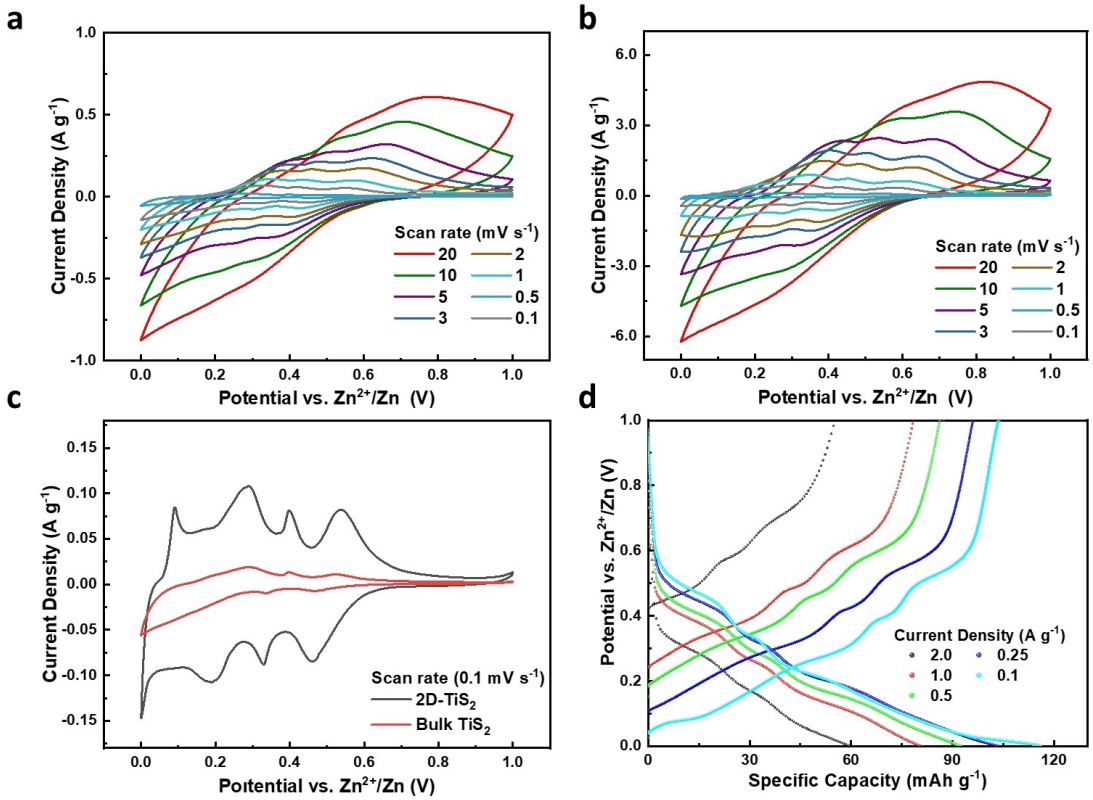

Figure 3. Electrochemical characterization of the TiS_2 structures. CV measurements of (a) bulk-TiS_2 and (b) 2D-TiS_2 at various scan rates. (c) Comparison of 2D and bulk TiS_2 ZnCs CV curves at a scan rate of 0.1 mV s^{-1}. (d) GCD measurements of 2D-TiS_2-based ZnCs at different current densities and relevant capacities.

density of 0.1 A g^{-1}, showing ideal storage properties for Zn-ion-based energy storage solutions.

Figure 4 shows the ex-situ XRD patterns of the 2D-TiS_2 during charging and discharging. Devices were held at

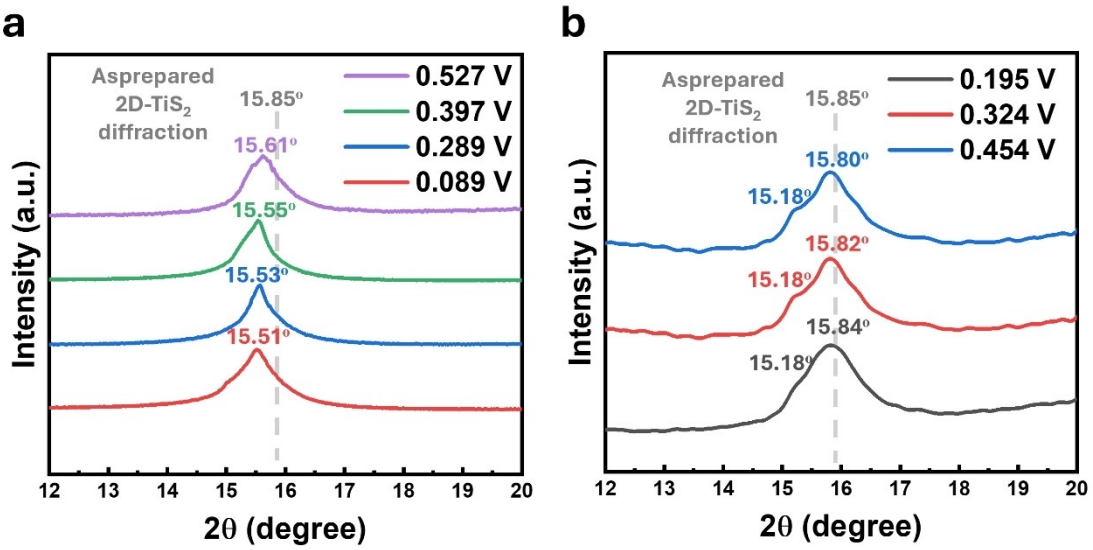

Figure 4. Ex-situ XRD analysis of 2D-TiS_2-based ZnCs following (a) charging and (b) discharging.

potentials observed in Figure 3d, where redox peaks were observed. After a couple of CV cycles, the 2D-TiS_2-based ZnCs were kept at specific voltages for 5 minutes to ensure the completion of reactions. The cells were then disassembled, and 2D-TiS_2 electrodes were taken to XRD for ex-situ analysis. In Figure 4a, the XRD peaks were located at 15.51, 15.53, 15.55, and 15.61°, corresponding to right after being charged to 0.527, 0.397, 0.298, and 0.089 V, respectively. Whereas, in Figure 4b all the XRD peaks corresponding to 0.195 V, 0.324 V, and 0.454 V during discharging are located at 15.84, 15.82, and 15.80°, respectively. During charging, the Zn^{+2} ions are intercalated into the 2D-TiS_2 structure, forming Zn_xTiS_2 where *x* can reach up to 1. As seen from Figure 4a, as the Zn^{+2} ions were inserted, the XRD patterns shifted to lower degrees, indicating the expansion of 2D-TiS_2 layers during Zn^{+2} ion intercalation.[75] This shift became larger as more Zn^{+2} ions were inserted, as expected. During the discharge, Zn^{+2} ions were deintercalated from the 2D-TiS_2 layers, which increased the (001) diffraction angle almost at the original value of 15.85°. Yet, secondary diffraction, which was at a much lower diffraction angle, 15.18°, became visible, which can be due to the irreversible expansion of some layers during charge-discharge cycles as reported in the literature as a result of remaining Zn within the structure.[72,73]

Impedance measurements are valuable to understanding the mechanism of the energy storage devices. Potentiostatic impedance measurements (PEIS) are generally utilized to obtain Nyquist graphs, yet they fall short of differentiating between the capacitive, pseudocapacitive, and battery-like behaviors.[70,76] Therefore, a staircase potentiostatic impedance analysis (SPEIS) was conducted on the 2D-TiS_2-based ZnCs to fully obtain 3D Bode Plots to understand the energy storage mechanism fully. 20 steps of SPEIS ranging from 0.25 to 1.0 V are taken with the frequency range of 100 kHz to 10 mHz and 10 mV sinus amplitude. Relevant 3D plots were provided in Figure 5. Figure 5a shows the change in the real-specific capacitance, C', with respect to changing potentials and frequency. A maximum

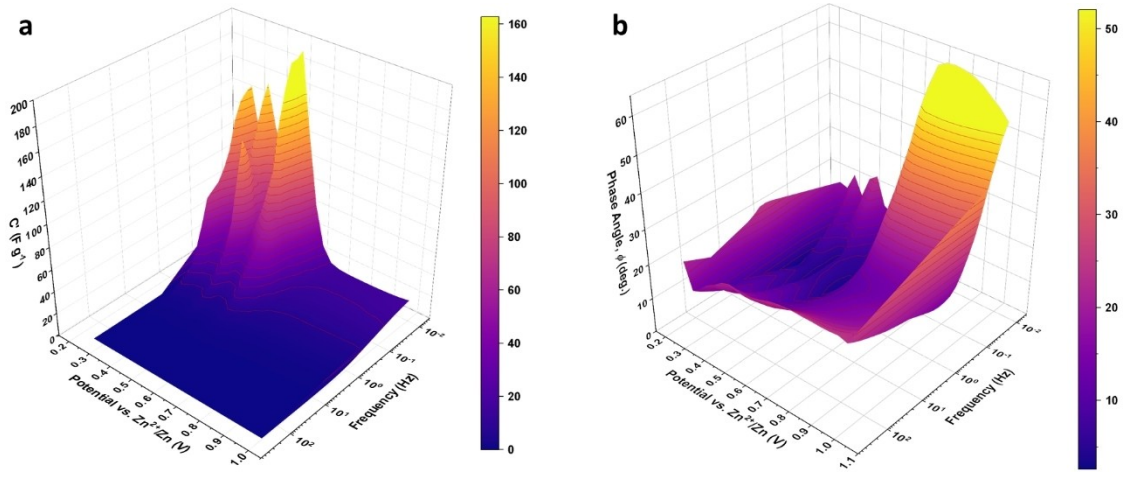

Figure 5. 3D Bode plots of 2D-TiS_2-based ZnCs. (a) real-gravimetric capacitance vs. frequency vs potential, and (b) phase angle (φ) vs. potential vs. frequency.

real-gravimetric capacitance of 194.06 F g^{-1} at the potential of 0.52 V and 10 mHz is observed, followed by again local maximums at 0.48 V, 0.36 V, and 0.29 V. The maximum real-gravimetric capacitance is in a well agreement with the specific capacitance found from the CV (214.3 F g^{-1}) provided in Figure 3c, indicating the reliability of the 3D Bode plot. Moreover, a direct correlation between the redox peaks in CV measurement and the potentials of the maximum real-gravimetric capacitances in Figure 5a can be observed. Up to the higher frequencies of almost 1 Hz can be observed, which indicates the pseudocapacitive behavior of the 2D-TiS_2. This can also be proven with the 3D Bode plot of Phase Angle (φ) concerning the potential and frequency (Figure 5b). A wide area of $\varphi < 30^\circ$ directly indicates a resistive behavior that can be correlated with the pseudocapacitive mechanism. It is important to note that for simple electrochemical double-layer capacitors (EDLCs), φ tends to be $> 70^\circ$ at lower frequencies, which do not change with applied potential. At higher voltages, φ becomes larger than 50°, indicating only a double-layer capacitive region, which can again be correlated with the low current densities in Figure 3c at potentials > 0.6 V.[76] Overall, 3D Bode plots in Figure 5 demonstrate a well-discerned pseudocapacitive behavior dependent on the Zn^{2+} intercalation into 2D-TiS_2 layers.

For both maximum anodic (0.195 V) and cathodic (0.289 V) peak currents, current density vs. square root of scan rate plots were fitted (Figures 6a and 6c). Anodic and cathodic current R^2 values of 0.98 and 0.99 were obtained by linear fitting, indicating promising reversibility for both devices[77] Based on the plots provided in Figures 6b and 6d, *b*-values were calculated using Lindström's Method.[78] Even though redox peaks were observed at slow rates, the slope of *log* (scan rate) vs. *log* (current density) that corresponds to the b-value for 2D-TiS_2 and bulk TiS_2 using cathodic peak currents was found to be 0.85 and 0.87, respectively, showing a strong capacitive behavior in the charge storage mechanism. This can be related to the exfoliated nanosheets of TiS_2. 2D structure of the TiS_2 allow faster intercalation/deintercalation of Zn^{2+}, leading to a pseudocapacitive behavior. It is important to note that the ideal supercapacitor has a *b*-value of 1, while the ideal battery-type material has a *b*-value of 0.5.[79]

Since diffusion was expected to limit redox peaks, diffuse currents mainly occur within the peak regions.[80] The remaining sections of the CV were primarily capacitive. Dunn's method separated the surface-controlled (capacitive) current at the cathodic peak region from the overall current. In surface-controlled processes, the current is proportional to the scan rate; in diffusion-controlled processes, it is proportional to the

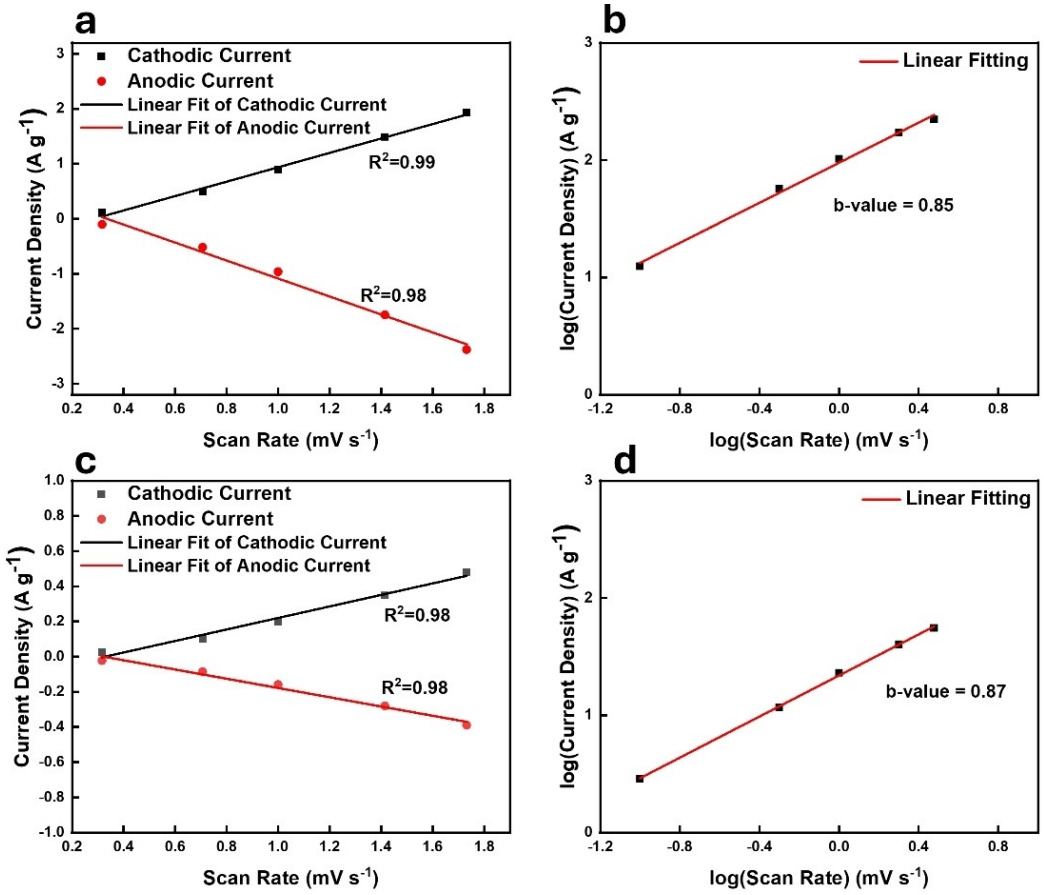

Figure 6. (a) The values of 2D-TiS_2 maximum anodic (0.195 V) and cathodic (0.289 V) peak current coefficient of determination (R^2). (b) The plot displaying the b-value of 2D-TiS_2 is the slope of the current density vs. log (scan rate). (c) Bulk TiS_2 anodic and cathodic current coefficient of determination (R^2) values. (d) The plot displaying the *b*-value of bulk TiS_2 is the slope of the current density vs. log (scan rate)

square root of the scan rate. Therefore, the following Equation 1 can be used to differentiate them.[81] There are distinct examples of usage of Dunn's method that differentiate the charge storage mechanisms in electrochemical devices.[82–84]

$$i(v) = k_1 v + k_2 v^{1/2} \quad (1)$$

The scan rate is represented by v in this equation, where $k_1 v$ and $k_2 v^{1/2}$ provide the capacitive and diffusive contributions, respectively. The equation above was divided by $v^{1/2}$ to produce a linear equation. k_1 and k_2 were obtained from the slope and intercept of $v^{1/2}$ vs $i(v)/v^{1/2}$ (Figure 7a and 7c). At a scan rate of 0.1 mV s^{-1}, the diffusive contribution was found to be 61.6% for 2D-TiS_2 (Figure 7b) and 50.1% for bulk TiS_2 (Figure 7e). The diffusion-controlled current was more prominent at lower scan rates, whereas at higher scan rates, the capacitive-controlled current took over (Figure 7c and f).

The stability test was conducted at scan rates of 0.1 and 1 A g^{-1} for 100 and 1000 cycles. When bulk TiS_2 exhibited an initial discharge capacity of 44.69 F g^{-1} and retained 53% of its capacity after 100 cycles at a scan rate of 0.1 A g^{-1}, devices using 2D-TiS_2 as the electrode material demonstrated a higher initial discharge capacity of 131.43 F g^{-1} but retained only 40% of their capacity after 100 cycles. At a higher scan rate of 1 A g^{-1}, bulk TiS_2 exhibited an initial discharge capacity of 4.13 F g^{-1}. It retained 57% of its initial capacity, whereas 2D-TiS_2 showed a 46.50 F g^{-1} initial discharge capacity and retained 41% of its initial capacity. Results clearly showed that 2D-TiS_2 showed remarkably higher initial discharge capacity but struggled with stability (Figure 8). When our results were

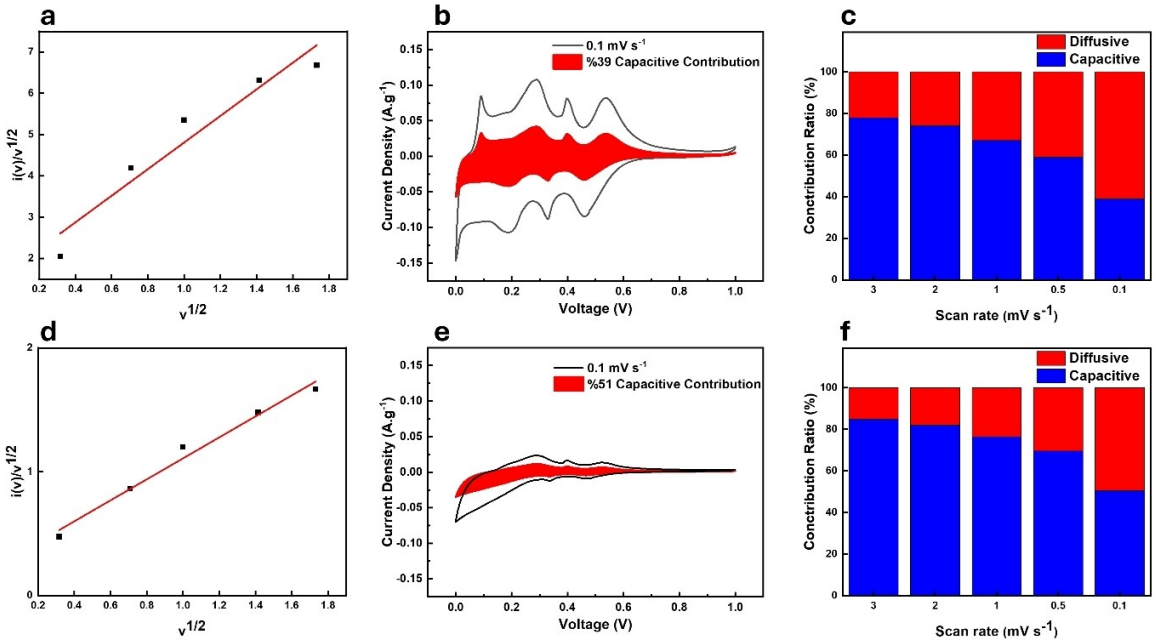

Figure 7. (a) Plot showing $v^{1/2}$ vs $i(v)/v^{1/2}$, which gives k_1 and k_2 values. (b) Capacitive contribution at a scan rate of 0.1 mV s^{-1}. (c) Amounts of the diffusive and capacitive contributions at various scan rates for 2D-TiS_2. (d) Plot showing $v^{1/2}$ vs $i(v)/v^{1/2}$ which gives k_1 and k_2 values. (e) Capacitive contribution at a scan rate of 0.1 mV s^{-1}. (f) Amounts of the diffusive and capacitive contributions at various scan rates for bulk TiS_2.

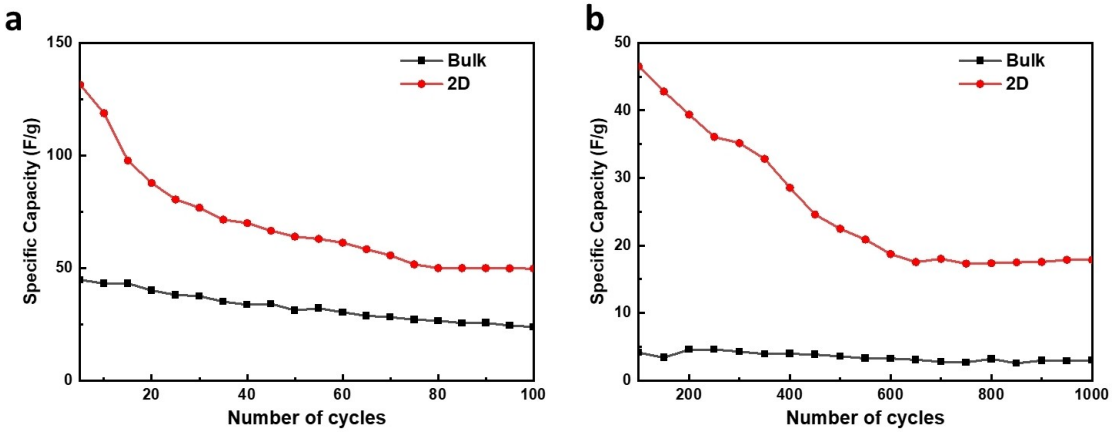

Figure 8. (a) Discharge capacities of bulk and 2D-TiS_2 at 0.1 A g^{-1} for 100 cycles, (b) Discharge capacities of bulk and 2D-TiS_2 at 1 A g^{-1} for 1000 cycles.

Table 1. ■■■Dear author, please mention the table heading. Thank you.■■■

Cathode and Anode	Electrolyte	Discharge Capacity ($mAh\,g^{-1}$)	Voltage (V)	Capacity Retention (Cycle Number)	Ref
PY14+-TiS_2/Zn	2 M $ZnSO_4$	130.9	0.05–1.0	84.3% (500)	85
TiS_2/Zn	$ZnSO_4$	120	0.05–1.0	70% (500)	71
$ZnMn_2O_4$/$Na0_{.14}TiS_2$	2 M $Zn(CF_3SO_3)_2$	105	0.05–1.0	74% (100)	86
2D-TiS_2/Zn	2M $ZnSO_4$	114.5	0.0–1.0	40% (100)	**Our work**
Bulk-TiS_2/Zn	2M $ZnSO_4$	44.7	0.0-1.0	53% (100)	**Our work**

compared with literature, we achieved the highest discharge capacity by using TiS_2 but struggled with stability as shown in Table 1

Conclusions

In conclusion, organolithium chemistry is used to exfoliate bulk TiS_2 powders prepared by annealing Ti and S powders. SEM, XRD, and XPS confirm the successful production of 2D-TiS_2 nanosheets. TiS_2 binder-free, self-standing, and electrically conductive electrodes are fabricated for utilization in ZnCs devices. A maximum specific capacitance of 214.3 $F\,g^{-1}$ based on CV analysis and a specific capacity of 116.4 $mAh\,g^{-1}$ based on GCD analysis is obtained, indicating the 2D-TiS_2 nanosheets are promising for Zn-ion-based aqueous energy storage devices. Compared to bulk TiS_2 with an initial discharge capacitance 44.69 $F\,g^{-1}$ at 0.1 $A\,g^{-1}$, the utilized 2D-TiS_2 electrode showed 131.43 $F\,g^{-1}$ and initial discharge capacity. Although with low-capacity retention, 2D-TiS_2 nanosheets still showed much higher capacitance values after degradation than the bulk TiS_2 structures. With continued research on the TiS_2, especially for mitigating its degradation, 2D-TiS_2 nanosheets can be driven forward for ZnCs and other aqueous Zn-ion-based energy storage devices.

Conflict of Interests

The authors declare no conflict of interest.

Data Availability Statement

The data that support the findings of this study are available from the corresponding author upon reasonable request.

Keywords: Titanium Disulfide (TiS_2) · Transition Metal Dichalcogenide (TMD) · aqueous zinc-ion capacitors

[1] M. Sengupta, Y. Xie, A. Lopez, A. Habte, G. Maclaurin, J. Shelby, *Renewable Sustainable Energy Rev.* **2019**, *89*, 51–60. doi: 10.1016/j.rser.2018.03.003.
[2] R. A. Kerr, *Science (80-).* **2007**, *316* (5822), 188–190. doi: 10.1126/science.316.5822.188.
[3] C. J. Rhodes, *Sci. Prog.* **2019**, *102* (1), 73–87. doi: 10.1177/0036850418823397.
[4] A. Hussain, S. M. Arif, M. Aslam, *Renewable Sustainable Energy Rev.* **2017**, *71 (July 2016)*, 12–28. doi: 10.1016/j.rser.2016.12.033.
[5] A. Whiteman, J. Esparrago, S. Rueda, SE and IA. *Renewable Capacity Statistics 2019, International Renewable Energy Agency (IRENA), Abu Dhabi.* **2019**. https://www.irena.org/publications/2019/Mar/Renewable-Capacity-Statistics-2019.
[6] X. Luo, J. Wang, M. Dooner, J. Clarke, *Appl. Energy* **2015**, *137*, 511–536. doi: 10.1016/j.apenergy.2014.09.081.
[7] B. K. Saikia, S. Maria, M. Bora, J. Tamuly, M. Pandey, *Fuel.* **2020**, *282 (April)*, 118796. doi: 10.1016/j.fuel.2020.118796.
[8] D. Lemian, F. Bode, F. Battery-Supercapacitor Energy Storage Systems for Electrical Vehicles: A Review. Published online 2022.
[9] Y. Qu, X. Zhang, N. Yang, X. Jiang, W. Lu, *J. Mater. Sci.* **2020**, *55* (34), 16334–16346. doi: 10.1007/s10853-020-05156-7.
[10] Z. Zhai, L. Zhang, T. Du, et al., *Mater. Des.* **2022**, *221*, 111017. doi: 10.1016/j.matdes.2022.111017.
[11] A. Riaz, M. R. Sarker, M. H. M. Saad, R. Mohamed, *Sensors.* **2021**, *21* (15).■■■Dear author please add pagenumbers or eLocator■■■ doi: 10.3390/s21155041.
[12] M. A. Bissett, S. D. Worrall, I. A. Kinloch, R. A. W. Dryfe, *Electrochim. Acta* **2016**, *201*, 30–37. doi: 10.1016/j.electacta.2016.03.190.
[13] X. Zang, C. Shen, E. Kao, et al., *Adv. Mater.* **2018**, *30* (5), 1–8. doi: 10.1002/adma.201704754.
[14] L. Wang, B. Chen, J. Ma, G. Cui, L. Chen, *Chem. Soc. Rev.* **2018**, *47* (17), 6505–6602. doi: 10.1039/c8cs00322j.
[15] D. Darbar, T. Malkowski, E. C. Self, et al., *Mater Today Energy.* **2022**, 30, ■■PF2■■101173. doi: 10.1016/j.mtener.2022.101173.
[16] S. Sun, J. Li, C. Xu, T. Zhai, Manganese-based layered oxides for electrochemical energy storage: a review of degradation mechanisms and engineering. Published online **2022**, 19231–19253.■■■Dear author, please add the volume number.■■■ doi: 10.1039/d2ta02242g.
[17] X. Wang, Q. Wei, H. Li, J. Sun, H. Li, Iron-chalcogenide-based electrode materials for electrochemical energy storage. Published online **2022**, 7517–7556.■■■Dear author, please add the volume number.■■■ doi: 10.1039/d1ta10930h.
[18] Z. Abbas, N. Hussain, S. Kumar, S. M. Mobin, *Nanoscale.* **2023**, *16* (2), 868–878. doi: 10.1039/d3nr04984a.
[19] X. Zhang, T. Cao, G. Zhang, et al., *J. Mater. Chem. A* **2024**, *12* (9), 4996–5039. doi: 10.1039/d3ta07372f.
[20] J. Zhu, C. Yan, G. Li, et al., *Energy Storage Mater.* **2024**, *65 (October 2023).*■■■Dear author please add pagenumbers or eLocator■■■ doi: 10.1016/j.ensm.2023.103111.
[21] S. Chen, L. Qiu, H. M. Cheng, *Chem. Rev.* **2020**, *120* (5), 2811–2878. doi: 10.1021/acs.chemrev.9b00466.
[22] J. Asenbauer, T. Eisenmann, M. Kuenzel, A. Kazzazi, Z. Chen, D. Bresser, *Sustain. Energy Fuels* **2020**, *4* (11), 5387–5416. doi: 10.1039/d0se00175a.
[23] A. Devendran, A. Nagai, *Mater Adv.* **2023**, *4* (12), 2524–2543. doi: 10.1039/d3ma00022b.
[24] S. W. Kim, D. H. Seo, X. Ma, G. Ceder, K. Kang, *Adv. Energy Mater.* **2012**, *2* (7), 710–721. doi: 10.1002/aenm.201200026.
[25] V. Augustyn, *J. Mater. Res.* **2017**.■■■Dear author please add pagenumbers or eLocator and the volume number■■■ doi: 10.1557/jmr.2016.337.
[26] S. Lu, L. Fang, X. Wang, et al., *Mater. Today Chem.* **2024**, *37 (December 2023)*, 101988. doi: 10.1016/j.mtchem.2024.101988.
[27] Y. You, X. L. Wu, Y. X. Yin, Y. G. Guo, *Energy Environ. Sci.* **2014**, *94* (7), 1643–1647. doi: 10.1039/c3ee44004d.
[28] B. Aydogdu, S. Aydin, S. P. Sasikala, H. E. Unalan, S. O. Kim, R. Yuksel, *J. Energy Storage* **2024**, *86 (PB)*, 111264. doi: 10.1016/j.est.2024.111264.

[29] C. Luo, H. Lei, Y. Xiao, et al., Recent development in addressing challenges and implementing strategies for manganese dioxide cathodes in aqueous zinc ion batteries. Published online **2024**.■■■Dear author please add pagenumbers or eLocator and the volume number■■■ doi: 10.20517/energymater.2023.119.
[30] Y. Sun, D. Chen, Z. Liang, *Mater Today Energy*. **2017**, *5*, 22–36. doi: 10.1016/j.mtener.2017.04.008.
[31] P. A. Shinde, A. M. Patil, S. Lee, E. Jung, S. Chan Jun, *J. Mater. Chem. A* **2022**, *10* (3), 1105–1149. doi: 10.1039/d1ta04642j.
[32] M. Narayanasamy, S. Zaman, C. M. Koo, *Mater Today Energy*. **2023**, *37*, 101405. doi: 10.1016/j.mtener.2023.101405.
[33] H. P. Hayat, F. K. Dokan, M. S. Onses, E. Yılmaz, A. Duran, E. Sahmetlioglu, *Mater. Res. Bull.* **2024**, *175 (July 2023)*, 112747. doi: 10.1016/j.materresbull.2024.112747.
[34] W. Fan, Q. Wang, K. Rong, et al., *Nano-Micro Lett.* **2024**, *16* (1).■■■Dear author please add pagenumbers or eLocator■■■ doi: 10.1007/s40820-023-01226-y.
[35] X. Li, Z. Huang, C. E. Shuck, G. Liang, Y. Gogotsi, C. M. Zhi, *Nat Rev Chem.* **2022**, *6* (6), 389–404. doi: 10.1038/s41570-022-00384-8.
[36] Y. Gogotsi, *Chem. Mater.* **2023**, *35* (21), 8767–8770. doi: 10.1021/acs.chemmater.3c02491.
[37] Z. Ali, T. Zhang, M. Asif, L. Zhao, Y. Yu, Y. Hou, *Mater. Today* **2020**, *35 (May)*, 131–167. doi: 10.1016/j.mattod.2019.11.008.
[38] S. Wu, Y. Du, S. Sun, *Chem. Eng. J.* **2017**, *307*, 189–207. doi: 10.1016/j.cej.2016.08.044.
[39] R. Yang, L. Mei, Q. Zhang, et al., *Nat. Protoc.* **2022**, *17* (2), 358–377. doi: 10.1038/s41596-021-00643-w.
[40] X. Qian, J. Liu, L. Fu, J. Li, *Science (80-).* **2014**, *346* (6215), 1344–1347. doi: 10.1126/science.1256815.
[41] D. Xia, F. Gong, X. Pei, et al., *Chem. Eng. J.* **2018**, *348 (February)*, 908–928. doi: 10.1016/j.cej.2018.04.207.
[42] V. V. Mohan, M. Manuraj, P. M. Anjana, R. B. Rakhi, *Energy Technol.* **2022**, *10* (3), 1–7. doi: 10.1002/ente.202100976.
[43] A. Eftekhari, *Appl Mater Today*. **2017**, *8*, 1–17. doi: 10.1016/j.apmt.2017.01.006.
[44] E. J. Frazer, S. Phang, P. Melbourne, *J. Power Sources* **1981**, *6*, 307–317.
[45] J. R. Owen, *Chem. Soc. Rev.* **1997**, *26*, 259–267.
[46] M. Li, J. Lu, Z. Chen, K. Amine, *Adv. Mater.* **2018**, *30* (1800561).■■■Dear author please add pagenumbers or eLocator■■■
[47] Y. Liu, H. Wang, L. Cheng, et al., *Nano Energy*. **2016**, *20*, 168–175. doi: 10.1016/j.nanoen.2015.12.028.
[48] H. Wang, Z. Qiu, W. Xia, et al., *J. Phys. Chem. Lett.* **2019**, *10* (22), 6996–7001. doi: 10.1021/acs.jpclett.9b02710.
[49] J. Zeb, X. Zhao, S. Ullah, M. G. Menezes, W. Zhang, *J. Mater. Sci.* **2021**, *56* (11), 6891–6902. doi: 10.1007/s10853-020-05760-7.
[50] C. Fang, R. de Groot, C. Haas, *Phys. Rev. B: Condens. Matter Mater. Phys.* **1997**, *56* (8), 4455–4463. doi: 10.1103/PhysRevB.56.4455.
[51] L. P. Zhao, G. Liu, P. Zhang, et al., *Chem. Pap.* **2019**, *73* (10), 2583–2589. doi: 10.1007/s11696-019-00812-y.
[52] W. Fan, F. Wang, X. Xiong, et al., *NPG Asia Mater.* **2024**.■■■Dear author please add pagenumbers or eLocator and the volume number■■■ doi: 10.1038/s41427-024-00537-9.
[53] T. Zhang, Y. Tang, S. Guo, et al., *Energy Environ. Sci.* **2020**, *13* (12), 4625–4665. doi: 10.1039/d0ee02620d.
[54] L. Wang, M. Jiang, F. Liu, et al., *Energy Fuels* **2020**, *34* (9), 11590–11596. doi: 10.1021/acs.energyfuels.0c02368.
[55] N. Zhang, X. Chen, M. Yu, Z. Niu, F. Cheng, J. Chen, *Chem. Soc. Rev.* **2020**, *49* (13), 4203–4219. doi: 10.1039/c9cs00349e.
[56] A. Deniz Ucar, S. Kandur, M. B. Durukan, et al., Overcoming Instability Challenges of Binder-Free, Self-Standing 1T-TiS 2 Electrodes in Aqueous Symmetric Supercapacitors Through Dopamine Functionalization. https://ssrn.com/abstract=4830505.
[57] Y. Cheng, A. Nie, Q. Zhang, L. Gan yong, Shahbazian-yassar R. Origin of the Phase Transition in Lithiated Molybdenum Disulfide. **2014**, *11*, 11447–11453.
[58] Q. Yun, Y. Ge, Z. Shi, et al., Recent Progress on Phase Engineering of Nanomaterials. Published online **2023**.■■■Dear author please add pagenumbers or eLocator and the volume number■■■ doi: 10.1021/acs.chemrev.3c00459.
[59] E. D. Grayfer, M. N. Kozlova, V. E. Fedorov, *Adv. Colloid Interface Sci.* **2017**, *245 (April)*, 40–61. doi: 10.1016/j.cis.2017.04.014.
[60] N. Sakhuja, R. K. Jha, R. Chaurasiya, A. Dixit, N. Bhat, *ACS Appl. Nano Mater.* **2020**, *3* (4), 3382–3394. doi: 10.1021/acsanm.0c00127.
[61] P. C. Sherrell, K. Sharda, C. Grotta, et al., *ACS Omega.* **2018**, *3* (8), 8655–8662. doi: 10.1021/acsomega.8b00766.
[62] K. Sun, Q. Zhang, D. C. Bock, et al., *J. Electrochem. Soc.* **2017**, *164* (6), A1291–A1297. doi: 10.1149/2.1631706jes.
[63] T. Liu, X. Zhang, M. Xia, et al., *Nano Energy*. **2020**, *67 (October 2019)*, 104295. doi: 10.1016/j.nanoen.2019.104295.
[64] H. Martinez, C. Auriel, D. Gonbeau, M. Loudet, *Appl. Surf. Sci.* **1996**, *93* (3), 231–235. doi: 10.1016/0169-4332(95)00339-8.
[65] J. C. Dupin, D. Gonbeau, I. Martin-Litas, P. Vinatier, A. Levasseur, *Appl. Surf. Sci.* **2001**, *173* (1–2), 140–150. doi: 10.1016/S0169-4332(00)00893-X.
[66] S. H. Overbury, D. R. Mullins, D. R. Huntley, L. Kundakovic, *J. Phys. Chem. B* **1999**, *103* (51), 11308–11317. doi: 10.1021/jp992240a.
[67] M. Telkhozhayeva, B. Hirsch, R. Konar, et al., *Appl Catal B Environ.* **2022**, *318 (May)*, 121872. doi: 10.1016/j.apcatb.2022.121872.
[68] Y. Wang, Z. Sofer, J. Luxa, M. Pumera, *Adv. Mater. Interfaces* **2016**, *3* (23), 1–8. doi: 10.1002/admi.201600433.
[69] S. A. Etghani, E. Ansari, S. Mohajerzadeh, *Sci. Rep.* **2019**, *9* (1), 1–14. doi: 10.1038/s41598-019-53651-y.
[70] W. J. Lee, Y. M. Sung, *Cryst. Growth Des.* **2012**, *12* (11), 5792–5795. doi: 10.1021/cg301317j.
[71] L. Wang, M. Jiang, F. Liu, et al., *Energy Fuels* **2020**, *34* (9), 11590–11596. doi: 10.1021/acs.energyfuels.0c02368.
[72] H. Tao, M. Zhou, R. Wang, K. Wang, S. Cheng, K. Jiang, *Adv. Sci.* **2018**, *5* (11).■■■Dear author please add pagenumbers or eLocator■■■ doi: 10.1002/advs.201801021.
[73] C. Huang, Y. Liu, J. Li, et al., *J. Mater. Sci. Technol.* **2023**, *140*, 135–141. doi: 10.1016/j.jmst.2022.09.012.
[74] Z. Hu, Z. Song, Z. Huang, et al., *Angew Chemie - Int Ed.* **2023**, *62* (38).■■■Dear author please add pagenumbers or eLocator■■■ doi: 10.1002/anie.202309601.
[75] B. Tian, W. Tang, K. Leng, et al., *ACS Energy Lett.* **2017**, *2* (8), 1835–1840. doi: 10.1021/acsenergylett.7b00529.
[76] J. S. Ko, C. H. Lai, J. W. Long, D. R. Rolison, B. Dunn, J. Nelson Weker, *ACS Appl. Mater. Interfaces* **2020**, *12* (12), 14071–14078. doi: 10.1021/acsami.0c02020.
[77] S. K. Babu, J. J. D. Raj, T. Vijayakumar, B. Gunasekaran, *Colloids Surfaces A Physicochem Eng Asp.* **2022**, *655 (July)*, 130244. doi: 10.1016/j.colsurfa.2022.130244.
[78] T. Schoetz, L. W. Gordon, S. Ivanov, A. Bund, D. Mandler, R. J. Messinger, *Electrochim. Acta* **2022**, *412 (February)*, 140072. doi: 10.1016/j.electacta.2022.140072.
[79] S. Pervez, M. Z. Iqbal, *Small.* **2023**, *19* (48).■■■Dear author please add pagenumbers or eLocator■■■ doi: 10.1002/smll.202305059.
[80] G. A. Muller, J. B. Cook, H. S. Kim, S. H. Tolbert, B. Dunn, *Nano Lett.* Published online **2015**.■■■Dear author please add pagenumbers or eLocator and the volume number■■■ doi: 10.1021/nl504764m.
[81] X. Li, L. Yuan, R. Liu, et al., *Adv Energy Mater.* Published online **2021**.■■■Dear author please add pagenumbers or eLocator and the volume number■■■ doi: 10.1002/aenm.202003010.
[82] T. S. Mathis, N. Kurra, X. Wang, D. Pinto, P. Simon, Y. Gogotsi, *Adv. Energy Mater.* **2019**, *9* (39), 1–13. doi: 10.1002/aenm.201902007.
[83] Y. Gogotsi, R. M. Penner, *ACS Nano.* **2018**, *12* (3), 2081–2083. doi: 10.1021/acsnano.8b01914.
[84] P. Simon, Y. Gogotsi, *Nat. Mater.* **2020**, *19* (11), 1151–1163. doi: 10.1038/s41563-020-0747-z.
[85] C. Huang, Y. Liu, J. Li, et al., *J. Mater. Sci. Technol.* **2023**, *140*, 135–141. doi: 10.1016/j.jmst.2022.09.012.
[86] W. Li, K. Wang, S. Cheng, K. Jiang, *Adv. Energy Mater.* **2019**, *9* (27).■■■Dear author please add pagenumbers or eLocator■■■ doi: 10.1002/aenm.201900993.

Manuscript received: November 30, 2024
Revised manuscript received: January 30, 2025
Version of record online: ■■, ■■

RESEARCH ARTICLE

This study explores two-dimensional titanium disulfide (2D-TiS_2) nanosheets as cathodes for zinc-ion capacitors (ZnCs). Organolithium exfoliation enhances TiS_2's electrochemical properties, improving capacitance and Zn^{2+} ion intercalation compared to bulk. Binder-free, self-standing 2D-TiS_2 electrodes offer a promising energy storage solution, advancing next-generation Zn-ion capacitors for efficiency and sustainability.

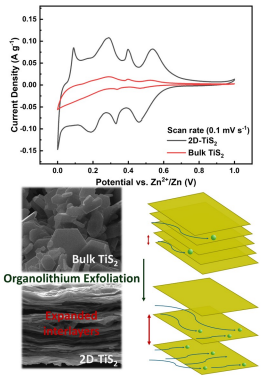

*S. K. Baglicakoglu, S. Oz, A. D. Ucar, Y. Kocak, M. B. Durukan, E. Ozensoy, H. E. Unalan**

1 – 11

Two-Dimensional Titanium Disulfide Nanosheets for Enhanced Capacity of Zinc-Ion Capacitors

SPACE RESERVED FOR IMAGE AND LINK

Share your work on X! ChemElectroChem promotes selected articles on X (formerly known as Twitter). Each article post contains the title, name of the corresponding author, a link to the article, selected handles and hashtags, and the ToC picture. If you, your team, or your institution have an X account, please include its handle @username below. We recommend sharing and interacting with these posts through your personal and/or institutional accounts to help increase awareness of your work! Please follow us @Chem_Europe.

ORCID (Open Researcher and Contributor ID)

Please check that the ORCID identifiers listed below are correct. We encourage all authors to provide an ORCID identifier for each coauthor. ORCID is a registry that provides researchers with a unique digital identifier. Some funding agencies recommend or even require the inclusion of ORCID IDs in all published articles, and authors should consult their funding agency guidelines for details. Registration is easy and free; for further information, see http://orcid.org/.

Sumeyye Kandur Baglicakoglu
Sena Oz
Ali Deniz Ucar
Yusuf Kocak
Mete Batuhan Durukan http://orcid.org/0000-0001-7714-9012
Emrah Ozensoy
Husnu Emrah Unalan http://orcid.org/0000-0003-3667-179X